Supersymmetry at the NLC

M. N. Danielson, S. Fahey, E. Goodman, U. Nauenberg, D. L. Wagner, B. Williams
University of Colorado, Boulder, Colorado, USA
H. Baer, R. Munroe
Florida State University, Tallahassee, Florida, USA
K. Fujii, M. Nojiri
KEK National Laboratory, Tsukuba, Japan
X. Tata
University of Hawaii, Honolulu, Hawaii, USA
J. L. Feng
Lawrence Berkeley Laboratory, Berkeley, California, USA
F. Cuypers
Paul Scherrer Institute
D. Burke, R. Dubois, M. E. Peskin, D. Pierce, J. D. Wells
Stanford Linear Accelerator Center, Stanford, California, USA
M. Drees
University of Wisconsin, Madison, Wisconsin, USA
S. Manly
Yale University, New Haven, Connecticut, USA

ABSTRACT

This paper explores the potential for studying supersymmetry (SUSY) at the Next Linear Collider. The NLC is not only a discovery machine, but can also be used to make detailed measurements of SUSY particle properties. We show why the NLC is a vital machine for this area of research by describing a number of analysis techniques that we use, and then illustrating this potential by analyzing simulated data from one specific model.

I. INTRODUCTION

The NLC can be used to perform many useful studies of supersymmetry in a clean and simple manner; in particular:

- It allows the discovery and the measurement of the particle mass spectrum predicted by SUSY, and
- It allows one to measure the cross sections, branching ratios and production angle distributions, which lead to the determination of the soft breaking and Higgsino mass parameters and the couplings of the SUSY particles (sparticles).

The NLC has many useful features that help in the study of supersymmetry. These include:

- The large electron longitudinal polarization.
- The beam energy can be tuned to optimize analysis.
- A high signal to background ratio which allows measurements of masses, differential cross sections and relative branching ratios.

A. Sparticle Discovery and Mass Measurements

The various aspects of supersymmetry and the properties of the SUSY particle spectrum based on the minimal SUGRA model (with its assumptions about the universal supersymmetry parameters at the high scale) has been described elsewhere [1,2]. If R-parity is conserved, as the models assume, then sparticles are produced in pairs and the lightest supersymmetric particle (LSP) at the end of the decay chain escapes the detector unobserved, carrying away a large fraction of the initial energy. This characteristic of the production of sparticles and the fact that the center of mass energy is very well known in e^+e^- annihilation leads to a very clean separation of the signal from the standard model (SM) processes. This allows accurate sparticle mass determinations using the endpoint of the energy spectrum of the observed particles from the sparticle decays, as shown in section III.B.

B. Sparticle Production Measurements

The cross sections and production angular distributions of sparticles have been calculated [3]. Computer simulations show clearly how these can be related to the angular distributions of observed decay particles [4].

C. Electron Polarization

The ability to polarize the electron beam is extremely useful in the analysis of SUSY. Electron beam polarization of 80% has

already been achieved at the SLC. For this study, we conservatively assume that there will be no improvements and that the positron beam cannot be polarized. The polarization can be used to vary the cross section of sparticles; in particular right-handed (left-handed) electrons can be used to enhance the production of right-handed (left-handed) selectron pairs. This effect is crucial for the measurement of the $U(1)$ and $SU(2)$ couplings; comparison with the standard model is a critical test of supersymmetry. The polarization can also be used to disentangle the contributions from different components of a mixed object. In addition, right-handed electrons can be used to reduce the standard model backgrounds, as discussed in more detail in section III.C.

D. Analysis Optimization

Due to the soft breaking parameters and D-terms that are present in SUSY the sparticle mass spectrum may have splittings of the order of tens of GeV's. Hence, in principle, many of the sparticles are produced simultaneously with similar decay signals. Nevertheless, a judicious choice of the collision energy can enhance the production of one sparticle over the other. For example, in the case of point 3 of our parameter space discussed in section II.A, the masses of the right-handed and left-handed selectrons are different by 9 GeV. Hence, tuning the collision energy and the electron polarization can enhance markedly the production of one sparticle over the other.

E. Signal over Background

In the SUGRA model, SUSY particles are produced in pairs and decay into the LSP, which is heavy and escapes detection. This leads to large missing energy and large angle, make the e^+e^- collider environment particularly valuable. The standard model processes like W^+W^- pair production and 2-γ processes have quite different characteristics. Therefore the SUSY production can be separated from these other processes leading to a high signal to background ratio.

Figure 1 shows the distribution of visible energy for point 3 SUSY and SM W^+W^- events before and after the cuts described in section III.A. There is a large enhancement of the signal events over the SM background, which is mainly due to W^+W^- final states.

II. SUPERSYMMETRY SIMULATION

The study of the capabilities of the NLC is based on the analysis of simulated events. We use ISAJET 7.22 [5] to generate the supersymmetric events and the W^+W^- background events since they are sensitive to the electron longitudinal polarization and the program includes this dependence; we use PYTHIA 5.7 [6] and SPYTHIA 2.05 [7] to generate other backgrounds, mainly 2-γ processes since they are not sensitive to the electron polarization and these processes are not in ISAJET. We also use SPYTHIA to determine the effect of bremsstrahlung on the mass measurement resolution, as described in section II.B.3. In this section we discuss the SUSY models that were studied and describe the simulation programs used.

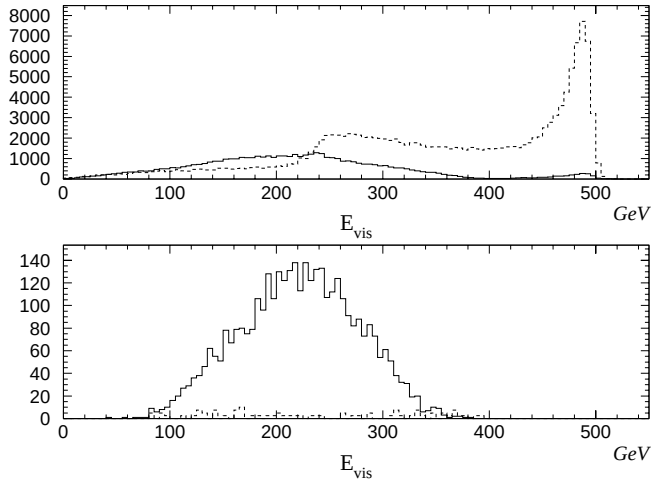

Figure 1: The distribution of total visible energy for SUSY (solid curve) and SM W^+W^- (dashed curve) events before and after a series of cuts described in section III.A. The events were generated at $\sqrt{s} = 500$ GeV with 80% right-polarized electrons. The signal to background ratio is about 30-to-1 after the cuts.

A. Parameter Sets

We chose to study five SUSY parameter sets that represent such diverse scenarios of particle production that analyzing them all would be representative of the capabilities of a Linear Collider. The parameters are given in Table I. Four of these are within the "minimal supergravity" or "SUGRA" framework, with a universal scalar mass (m_0) and a universal gaugino mass ($m_{1/2}$) as well as a universal scalar trilinear coupling parameter (A_0), all defined at the GUT scale [1, 2]. The resulting mass values are shown in Figure 2.

The parameters were chosen to emphasize different sparticle production:

Point 1 Chargino production
Point 2 Slepton production
Point 3 Charginos and sleptons
Point 4 Higgsino-like chargino and additional Higgs bosons
Point 5 Light stop production

Table I: List of values for the five parameter sets ("points"). All masses are given in GeV. (In this report, the top quark mass is taken to be 175 GeV.)

Parameter	1	2	3	4[a]	5
m_0	400	100	200	*	300
$m_{1/2}$	200	300	100	*	150
A_0	0	0	0	*	-600
$\tan(\beta)$	2	2	2	10	2
$\mathrm{sign}(\mu)$	-1	-1	-1	-1	1

[a] For point 4, the other parameters are: $\mu = -100$, $m_{\tilde{g}} = 900$, $m_{\tilde{f}} = 1000$, $A_b = A_t = -1000$.

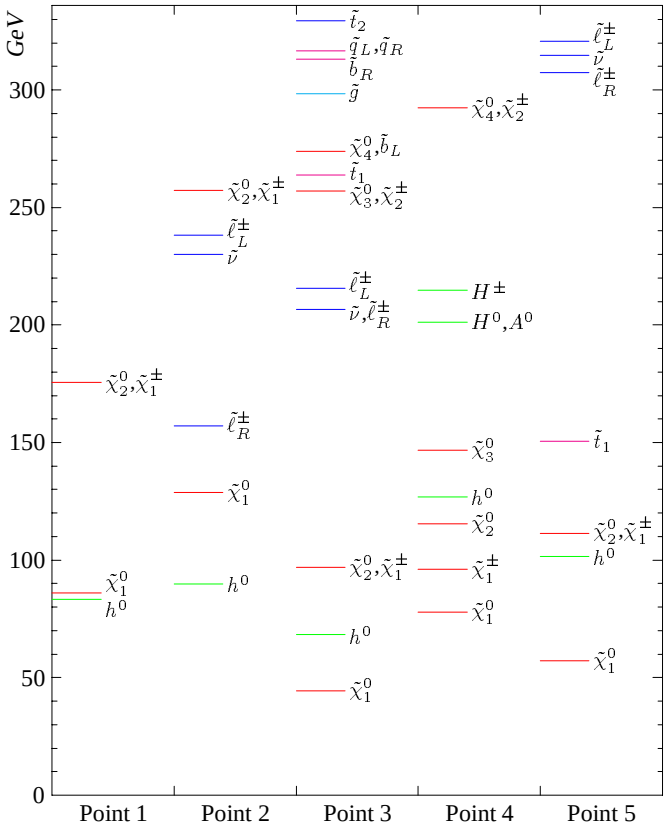

Figure 2: Mass spectra of particles for the five parameter sets ($\widetilde{q}$ represents only the first- and second-generation squarks).

Point 3, also known as the comparison point, also has been studied by the TeV33 and LHC subgroups. This point is characterized by the fact that most of the sparticle masses are low and can be produced in all the accelerators discussed at this conference. All the particles are produced at once, making the study more complicated. The NLC is particularly useful in this case because, as discussed above, the energy of the machine can be tuned to observe particular signals.

Although we have chosen to study parameter sets within the SUGRA model, we note that the evaluation of the SUSY discovery capabilities is largely insensitive to our choice. In fact, precision studies with the NLC will also serve to stringently test the assumptions underlying the SUGRA framework.

Table II lists the numbers of particles produced in some of the channels for the five parameter sets in one year of running at design luminosity (50 fb^{-1}yr^{-1}). No matter which parameter set describes nature, NLC 500 ($\sqrt{s} = 500$ GeV) will be able to produce thousands of supersymmetric events. Because of this and because of the high signal to background we can measure the masses, cross sections and branching ratios to a high precision.

B. Simulation Program

We use the ISAJET 7.22 event generator program to simulate supersymmetry. The SUGRA framework has been incorporated into ISAJET [8], as have all lowest order $e^+e^- \to 2$ sparticle and Higgs boson production mechanisms. These include the following processes [9] (here, as in the rest of this document, we neglect bars over anti-particles):

$$\begin{aligned} e^+e^- &\to \widetilde{q}_L\widetilde{q}_L,\ \widetilde{q}_R\widetilde{q}_R, \\ &\to \widetilde{\ell}_L\widetilde{\ell}_L,\ \widetilde{\ell}_R\widetilde{\ell}_R, \\ &\to \widetilde{\nu}_\ell\widetilde{\nu}_\ell, \\ &\to \widetilde{\chi}_1^+\widetilde{\chi}_1^-,\ \widetilde{\chi}_2^+\widetilde{\chi}_2^-,\ \widetilde{\chi}_1^+\widetilde{\chi}_2^- + c.c., \\ &\to \widetilde{\chi}_i^0\widetilde{\chi}_j^0,\ (i,j = 1\text{–}4), \\ &\to Z^0h^0,\ Z^0H^0,\ A^0h^0,\ A^0H^0,\ H^+H^-. \end{aligned}$$

Table II: Numbers of events produced for selected channels for each of the five parameter sets at $\sqrt{s} = 500$ GeV with 80% right-handed electron polarization with one year (50 fb^{-1}) of data.

Production mode	1	2	3	4	5
$\widetilde{\chi}_1^+\widetilde{\chi}_1^-$	6600		7950	13600	7700
$\widetilde{\chi}_1^0\widetilde{\chi}_2^0$	500	700	2850	7400	1100
$\widetilde{\chi}_2^0\widetilde{\chi}_2^0$	400		1650	50	1850
$\widetilde{\nu}_e\widetilde{\nu}_e$		1550	12600	13700	
$\widetilde{e}_R^+\widetilde{e}_R^-$		14000	12150		
$\widetilde{e}_L^+\widetilde{e}_L^-$		100	2200		
$\widetilde{t}_1\widetilde{t}_1$					3300
h^0Z^0	2900	2900	2950	2600	2800

All squarks and sleptons other than staus and stops are taken to be L or R eigenstates. (For the stops, $\widetilde{t}_1\widetilde{t}_1$, $\widetilde{t}_1\widetilde{t}_2$ and $\widetilde{t}_2\widetilde{t}_2$ are produced, where $\widetilde{t}_{1,2}$ are the top squark mass eigenstates.)

Given a point in SUGRA space and a collider energy, ISAJET generates all allowed production processes according to their relative cross sections. The produced sparticles or Higgs bosons are then decayed into all kinematically accessible channels, with branching fractions calculated within ISAJET. The sparticle decay cascade terminates with the stable LSP, taken to be the lightest neutralino ($\widetilde{\chi}_1^0$). Final state QCD radiation is included, as well as particle hadronization. ISAJET currently neglects spin correlations, sparticle decay matrix elements, initial state photon radiation and beamsstrahlung effects. In the above reactions, spin correlation effects are only important for chargino and neutralino pair production, while decay matrix elements are only important for three-body sparticle decays.

1. *Polarization*

To facilitate investigation of polarized beam effects on signal and background cross sections, particle production via polarized beams has been included in the ISAJET e^+e^- cross sections [10]. The degree of longitudinal beam polarization is parametrized as

$$P_L(e^-) = f_L - f_R$$

where

$$f_L = \frac{n_L}{n_L + n_R} = \frac{1 + P_L}{2} \text{ and}$$

$$f_R \quad = \quad \frac{n_R}{n_L + n_R} = \frac{1 - P_L}{2} \; .$$

In the above, $n_{L,R}$ is the number of left (right) polarized electrons in the beam, and $f_{L,R}$ is the corresponding fraction. An 80% right polarized beam corresponds to $P_L(e^-) = -0.6$ and a completely unpolarized beam corresponds to $P_L(e^-) = 0$.

The inclusion in the simulation of the electron polarization is important because we need to understand its effect on our ability to sort out those signals which are topologically similar but come from different sparticle production mechanisms; we will see that these mechanisms can most simply be untangled by changing the longitudinal polarization of the electron beam. The use of this effect in uncovering the various signals is discussed in detail in section III.C.

2. *Detector simulation*

We apply resolution broadening to each four-vector in the final state according to the performance assumptions of the detector being considered. There is a 2% detection inefficiency for all particles, independent of momentum, and the beam hole covers the region $|\cos\theta| \geq 0.99$. The resolution parameters are listed in Table 2.2, page 25, of the NLC report submitted to Snowmass [11]. In addition, all photons with $E_\gamma < 0.5$ GeV as well as any charged particle with $p_T < 0.24$ GeV are considered unobservable.

3. *Beam energy*

One of the questions to be answered by simulation is the effect of bremsstrahlung on our ability to make accurate measurement of the masses of sparticles. These beam effects distort the center of mass energy of the production and therefore affect the endpoint energies of the decay particles that are being measured.

Since ISAJET includes neither initial state radiation nor beamstrahlung, we studied the distortion of the secondary particle energy spectrum due to these effects using SPYTHIA. We used the beam energy spectrum in the Zeroth-Order design report [12]. Figure 3 shows how the electron energy distribution from $\widetilde{e}_R^{\pm}$ decays changes when initial state radiation is turned on in the simulation. We note that the spectrum changes at the few percent level but in a systematic way that can easily be corrected by simulation techniques. Hence this should not affect adversely the accuracy of the mass measurements. Nevertheless, it requires knowing the colliding beam energy spectrum well.

At the same time these effects reduce the number of events observed and hence affect the precision that can be attained on the measurement of the cross section and therefore the determination of the coupling constants. Knowledge of the beam energy spectrum also allows us to correct for the apparent changes in the cross sections.

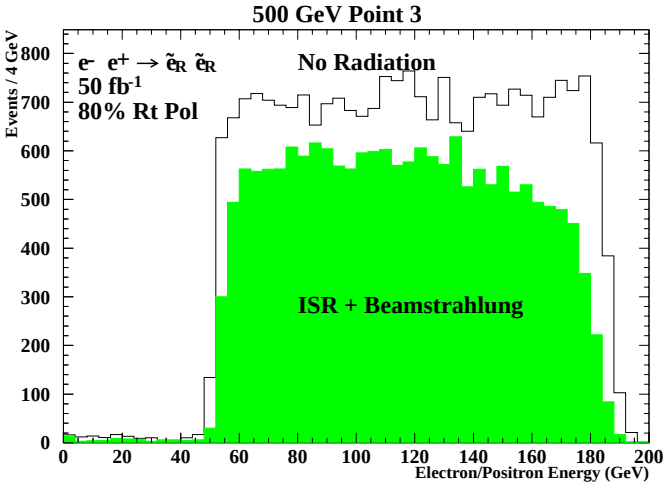

Figure 3: Effect of initial state radiation and beamstrahlung on the electron energy from $\widetilde{e}_R^{\pm}$ decays.

III. ANALYSIS METHODS

This section discusses various analysis tools that we will be using later on in section IV. We begin with a discussion of the event selection, followed by a description of the mass measurement technique and conclude with a discussion of the studies that can be performed using electron polarization.

A. Event selection

At the NLC, the signatures of supersymmetry events are significantly different from those of standard model events. This makes it easy to separate the signal from the background.

In this section, we discuss the separation of the SUSY signal from the background. We take as an example point 3 data generated at $\sqrt{s}$ = 500 GeV with 80% right-polarized electrons. Figure 4 shows the distributions of the quantities we will be cutting on to separate the SUSY signal from the W^+W^- background. We focus on W^+W^- events, since they are the primary source of the background; they are copiously produced (see Figure 10) and they often decay through modes with neutrinos (and thus missing energy). In this analysis, we calculate the thrust axis of the event and divide the event into two hemispheres; the forward hemisphere is defined to be the hemisphere that contains the greater energy. The cuts that we use for these plots are:

- $|\cos\theta_{thrust}| < 0.85$
- $E_{back} > 0$
- number of particles per jet ≥ 5
- $E_{for} < 0.4 E_{cm}$

These cuts are chosen to enhance the $\widetilde{\chi}_1^+\widetilde{\chi}_1^-$ events in which the $\widetilde{\chi}_1^{\pm}$ decays to $\widetilde{\chi}_1^0 q\overline{q}$. They eliminate standard model events, as well as some types of background from other SUSY channels.

The cut on $|\cos\theta|$ separates SUSY events from SM events; W^+W^- and Z^0Z^0 events tend to be highly peaked in the beam direction, while SUSY events are isotropically distributed in $\cos\theta$. The cut on $E_{back} > 0$ (i.e., the energy in the hemisphere with the lower energy) ensures that there is energy in both hemispheres of the event; this eliminates events that contain neutrinos such as Z^0Z^0 with one $Z^0 \to \nu\overline{\nu}$ and a large class of events such as $W \to \ell\nu$ where the lepton disappears down the beam

pipe. The cut on the number of particles per jet ensures that the jet comes from quarks and not from τ's or from leptonic decays of the W. The signature of SUSY is large missing energy; the cut on $E_{for} < 0.4E_{cm}$ eliminates all events with no missing energy (such $W^+W^- \to$ jets or h^0Z^0 events).

Figure 4 shows the four cut quantities after successive cuts; the plots are (a) the distribution of $|\cos\theta_{thrust}|$ for all events, (b) the energy in the backward hemisphere after the $|\cos\theta|$ cut, (c) the number of particles per jet after the E_{back} cut and (d) E_{for} after the cut on the number of particles per jet.

After these four cuts, the resulting visible energy distribution is as shown in Figure 1; the background is almost completely eliminated.

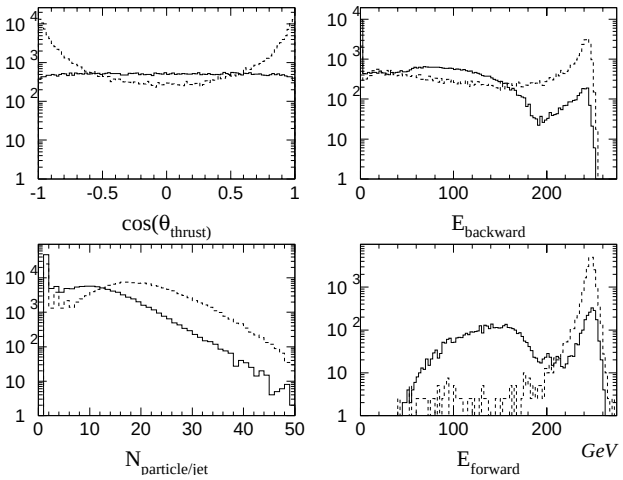

Figure 4: Distributions of cut variables, after successive cuts. The solid histogram is point 3 data, the dashed histogram is SM W^+W^- events.

B. Mass Measurements

In our studies, we assume that R-parity is conserved, which means that there will always be a lightest supersymmetric particle which will carry away significant amounts of energy.

Many supersymmetric particles will have 2-body decays, for example $\widetilde{e}^{\pm}_R \to \widetilde{\chi}^0_1 e^{\pm}$, as shown in Figure 5; in this case, the electron has a unique energy in the rest frame of the $\widetilde{e}^{\pm}_R$, and so its energy in the laboratory frame will have a box distribution, like that of Figures 3 and 15. We can calculate the endpoints of this distribution from the equation

$$E_{max,min} = (1 \pm \beta)\gamma E_{e,cm}$$

(here we have used the fact that $m_e \ll E_e$) and where

$$E_{e,cm} = \frac{m_{\tilde{e}}}{2}\left(1 - \frac{m^2_{\tilde{\chi}^0_1}}{m^2_{\tilde{e}}}\right)$$

and

$$\begin{aligned} \beta &= \left(1 - \frac{4m^2_{\tilde{e}}}{s}\right)^{\frac{1}{2}} \\ \gamma &= \frac{\sqrt{s}}{2m_{\tilde{e}}}. \end{aligned}$$

This leads to the results

$$\begin{aligned} m_{\tilde{e}} &= \sqrt{s}\left[\frac{E_{max}E_{min}}{(E_{max}+E_{min})^2}\right]^{\frac{1}{2}} \\ m^2_{\tilde{\chi}^0_1} &= m^2_e + s\left(\frac{E_{max}E_{min}}{E_{max}+E_{min}}\right) \times \\ &\qquad \left(\frac{1}{E_{max}+E_{min}} - \frac{2}{\sqrt{s}}\right). \end{aligned}$$

Although these expressions have been written for this particular decay, it should be clear that these apply to any two-body decay including those where the daughters decay further, e.g. $\widetilde{t}_1 \to b\widetilde{\chi}^+_1$, which has been used in Ref. [10] to obtain the chargino and t-squark mass.

We show below typical fits to energy spectra and the resulting mass determinations from the fits. We consider here only the results using point 3 in the SUGRA parameter space and a colliding energy of 500 GeV. These results have also been presented in the report submitted to Snowmass [11]. Figure 6 shows the energy distribution of electrons from $\tilde{\nu}_e$ decays that arise from the process $e^+e^- \to \widetilde{\nu}_e\widetilde{\nu}_e$ and the decay chain $\to e^-\widetilde{\chi}^+_1 e^+\widetilde{\chi}^-_1 \to e^-\mu^+\widetilde{\chi}^0_1 e^+\widetilde{\chi}^0_1$ + 2 jets or $\to e^-\widetilde{\chi}^0_1 e^+\mu^-\widetilde{\chi}^0_1$ + 2 jets. This data is based on 25 fb^{-1} integrated luminosity which is equivalent to a half year run at design luminosity using an 80% left-handed polarized electron beam. The fit to the edges of the energy distribution lead to mass measurements

$$\begin{aligned} m_{\tilde{\nu}_e} &= 207.5 \pm 2.5 \text{ GeV} \\ m_{\tilde{\chi}^+_1} &= 97.0 \pm 1.2 \text{ GeV} \end{aligned}$$

compared with the input values of 206.6 and 96.1 GeV respectively.

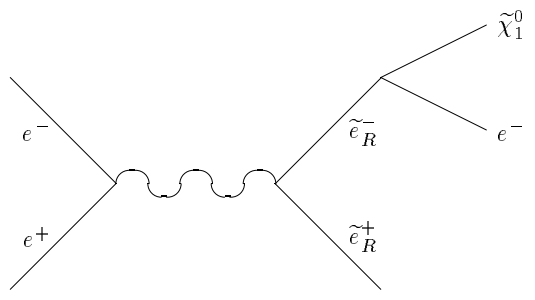

Figure 5: Diagram for the process $e^+e^- \to \widetilde{e}^+_R\widetilde{e}^-_R$ with $\widetilde{e}^-_R \to \widetilde{\chi}^0_1 e^-$.

Another possible measurement of mass can be done with three body decays. For example, for the case of the SUGRA point 5 in our parameter space, we can measure the $\tilde{\chi}^+_1$ and $\tilde{\chi}^0_1$ masses by studying the process $e^+e^- \to \tilde{\chi}^+_1\tilde{\chi}^-_1$ where both $\tilde{\chi}^{\pm}_1$ decay into $\tilde{\chi}^0_1 q\overline{q}$. At E_{cm} = 500 GeV and 80% left handed polarization

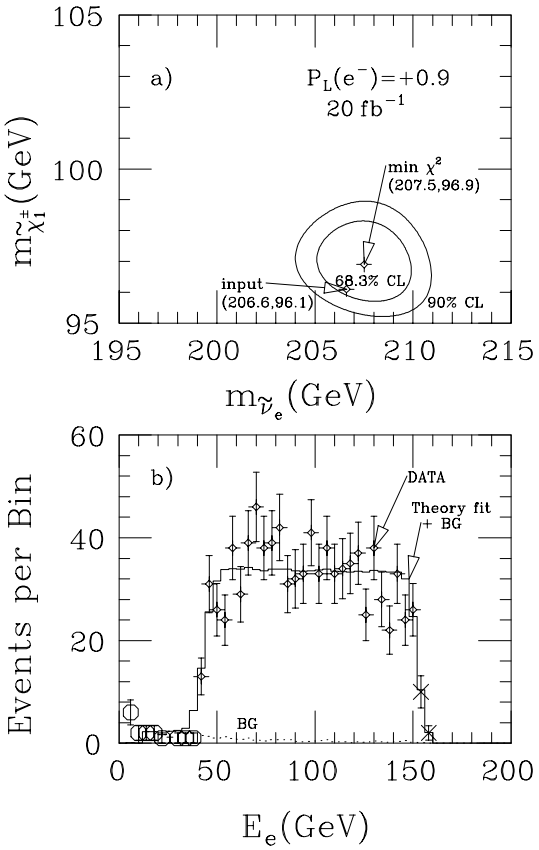

Figure 6: The electron energy distribution in the process $e^+e^- \to \tilde{\nu}_e\tilde{\nu}_e \to e^-\widetilde{\chi}_1^+e^+\widetilde{\chi}_1^- \to e^-\mu^\pm\widetilde{\chi}_1^0e^+\widetilde{\chi}_1^0$ + 2 jets and the fit that determines the mass of the $\widetilde{\nu}_e$= 207.5 ± 2.5 GeV and the mass of the $\widetilde{\chi}_1^+$ = 97.0 ± 1.2 GeV [10, 11].

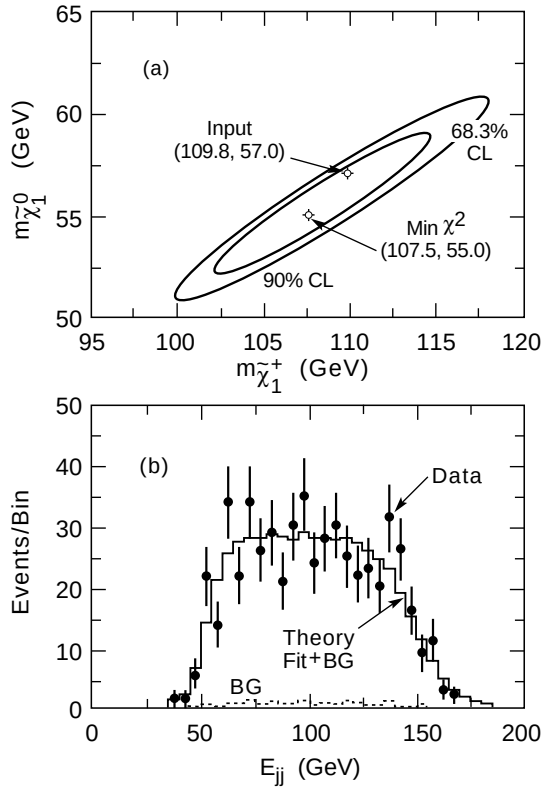

Figure 7: The jet-jet energy distribution in the process $e^+e^- \to \widetilde{\chi}_1^+\widetilde{\chi}_1^- \to \widetilde{\chi}_1^0q\overline{q}\widetilde{\chi}_1^0q\overline{q}$ and the fit to the $\widetilde{\chi}_1^+$ and $\widetilde{\chi}_1^0$ masses for point 5. We require M_{jj} to be near 30 GeV. The fits to the end point of the energy spectrum gives $m_{\tilde{\chi}_1^\pm}$ = 107.5 ± 6.5 GeV and $m_{\tilde{\chi}_1^0}$ = 55.0 ± 3.5 GeV [10, 11].

the production cross section is 850 fb. The branching ratio into $\tilde{\chi}_1^0$ and 2 jets (*jj*) is 65.8%; a typical one-year run at 50 fb^{-1} will produce over 18000 events. The resulting E_{jj} spectrum does not have a sharp endpoint behavior because of the 3-body nature of this decay. Hence we cannot use this spectrum to determine the masses accurately. But since the combined masses for the two jets, M_{jj}, does not vary much in this case we can simulate a two body process by keeping only events whose value of M_{jj} is near a given value. Figure 7 shows the E_{jj} distribution when M_{jj} is near 30 GeV. The fit to the energy spectrum leads to masses

$$m_{\tilde{\chi}_1^+} = 107.5 \pm 6.5 \text{ GeV}$$
$$m_{\tilde{\chi}_1^0} = 55.0 \pm 3.5 \text{ GeV}$$

compared with the input values of 109.8 and 57.0 GeV respectively.

C. Measurements using Polarization

The study of the production cross section of supersymmetric particles as a function of the longitudinal polarization of the electrons is of fundamental importance to understanding whether we are observing supersymmetry. Within the context of the SUGRA model the cross section of many of the supersymmetric particles varies markedly as we vary the polarization. This is because left-handed polarization enhances production via the *SU*(2)-like couplings and right-handed polarization enhances production via the *U*(1)-like couplings. Supersymmetry requires that these coupling constants be the same as those of the standard model. For those sparticles which are mixtures of the *SU*(2)- and *U*(1)-like particles, this technique allows us to measure the amount of mixing. Hence we can unravel the various first order Feynman diagrams responsible for these processes and determine the magnitude of the various coupling constants. This measurement is a crucial test of supersymmetry, independent of any model. We will also see examples of other measurements which allow us to test the additional assumptions behind the SUGRA framework, and specify the measurements that are necessary for these tests to be reliably carried out at the NLC. In this report we show how these cross sections vary assuming the SUGRA model is correct and indicate which sparticle productions need to be measured to make these tests.

Figure 9 shows the cross sections as a function of polarization for point 3 as generated by ISAJET (the Snowmass Report [11] and Ref. [10] show the corresponding plots for the other four points). This should be compared with Figure 10, which

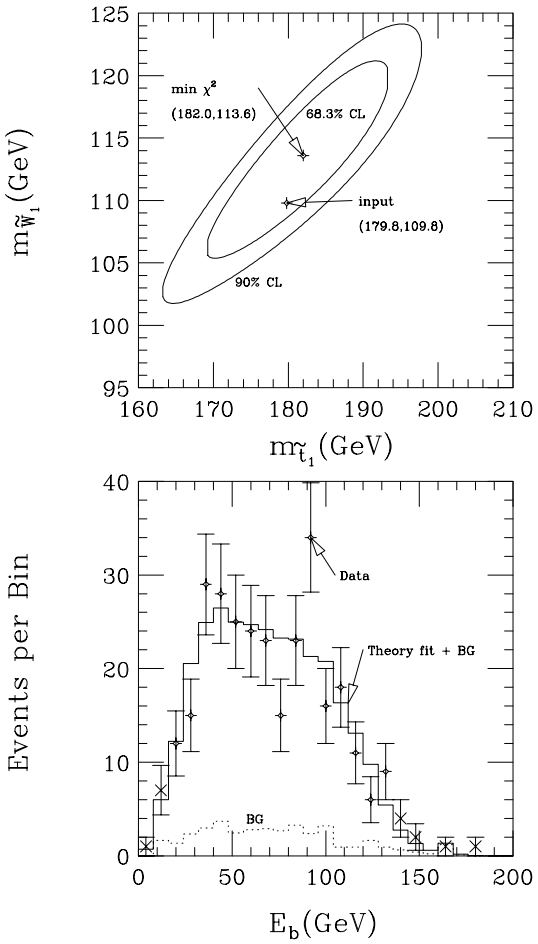

Figure 8: The b-jet energy distribution in the process $e^+e^- \to \widetilde{t}_1\overline{\widetilde{t}_1} \to b\widetilde{\chi}_1^+ b\widetilde{\chi}_1^-$ and the fit to the $\widetilde{t}_1\widetilde{\chi}_1^+$ masses. The fit gives the mass values $M_{\widetilde{t}_1} = 182 \pm 11$ GeV and $M_{\widetilde{\chi}_1^+} = 114 \pm 8$ GeV [10, 11].

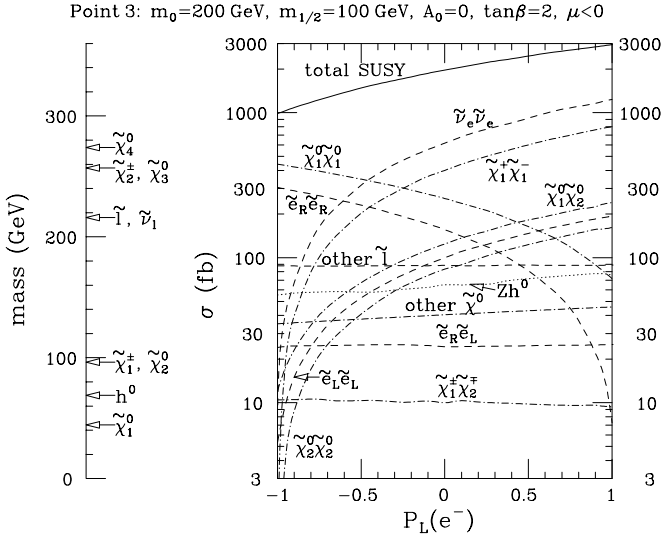

Figure 9: Cross sections of SUSY processes as a function of electron polarization for $\sqrt{s} = 500$ GeV, where $P_L(e^-) = 1.0$ corresponds to 100% left-handed polarization [3, 10].

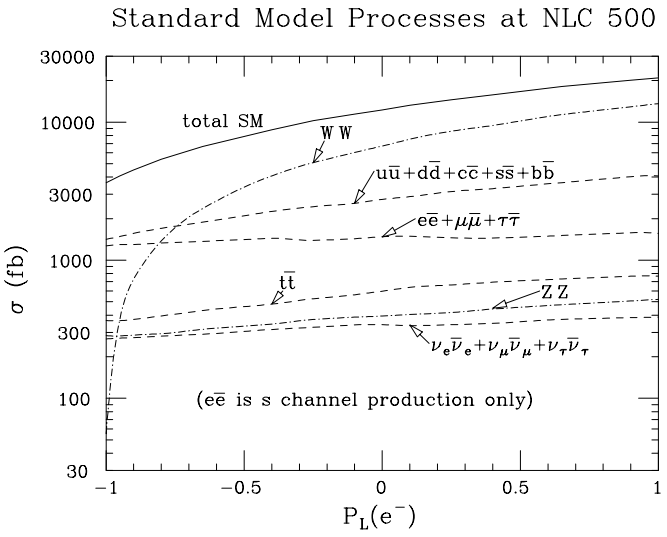

Figure 10: Cross sections of standard model processes as a function of electron polarization [3, 10].

shows the standard model processes. Many of these processes are backgrounds for SUSY since they can produce neutrinos that mimic the LSP. The background due to W^+W^- production can be significantly reduced by using right-polarized electrons.

We see from Figure 9 that $\widetilde{e}_L^{\pm}$ and $\widetilde{\nu}_e$ production dominates $\widetilde{e}_R^{\pm}$ production for left-handed electron polarization, while the opposite is true if the polarization is reversed.

In the case of $\widetilde{e}_{L,R}^{\pm}$ production one has two channels, the Z-γ s-channel process and the t-channel $\widetilde{\chi}_1^0$ exchange. The neutralinos, $\widetilde{\chi}_i^0$, are possibly mixtures of the bino ($\widetilde{B}^0$), wino ($\widetilde{W}^0$) and the two Higgsinos (which have neglible couplings to the incident beam). When the incident electron is right-handed, the production of $\widetilde{e}_R^{\pm}$ occurs via the s-channel exchange of γ and Z as well as via the bino part of the neutralinos exchanged in the t-channel. When the incident electron is left-handed, the production of $\widetilde{e}_L^{\pm}$ occurs via s-channel and via both the bino and wino parts of the neutralinos in the t-channel. Hence, by use of the electron polarization we can unravel the fraction of wino and bino that make up the neutralino, an important measurement needed to determine the validity of the SUGRA framework.

The $\widetilde{\nu}_e$ production also has two channels, the Z s-channel process and the t-channel $\widetilde{\chi}_1^{\pm}$ exchange. Since the the chargino is mainly a wino, the effects of electron polarization are even more clearly separated (the chargino's Higgsino component can be neglected because the magnitude of its coupling constant is proportional to the electron mass). If the incident electron is right handed the chargino t-channel does not contribute to $\widetilde{\nu}_e$ production. If the incident electron is left-handed it does contribute. Again this measurement is crucial to our understanding of the chargino and in confirming the SUGRA framework.

IV. MODEL-INDEPENDENT ANALYSIS

This section presents a model independent analysis as an example of what can be done at the NLC. For this example, we assign the parameters of the model to those of parameter set 3. Our analysis will be independent of this choice; the data will drive us to the conclusion that nature is described by the point 3 parameters, but the analysis should work regardless of which set of parameters is realized.

We measure the following quantities:

- Masses of the supersymmetric particles
- Left- and right-handed cross sections
- Branching ratios

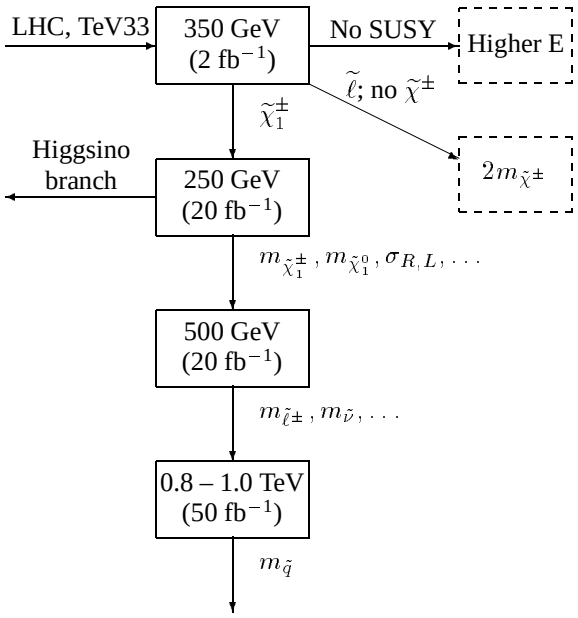

Figure 11: The steps of the analysis, assuming that nature is parametrized by point 3. The boxes show the CM energy and the minimum integrated luminosity to perform the measurements described in the text.

Figure 11 describes the steps that will be taken in this analysis. In real life, if nature is parametrized by point 3, we will have inputs from LEP2, LHC and TEV33 to guide us. In fact, for this particular example the lightest Higgs and the lightest neutralino will have been discovered, although this is not true for all possible SUSY parameters. The figure indicates the branches that would be taken if nature is described by parameters other than point 3. It also lists the minimum integrated luminosity needed at each energy to determine the SUSY parameters within reasonable errors, as described in the following sections.

A. 350 GeV

We start the analysis by assuming that we take data at 350 GeV. This energy approximately bifurcates the SUSY discovery space (and it also happens to be the $t\bar{t}$ threshold). If no SUSY particle is discovered at all, we search at a higher energy.

If the lightest neutralino and a right-handed slepton are discovered, but no chargino, then point 3 is ruled out and we run the NLC at $4m_{\tilde{\chi}_1^0}$ (assuming the unification of gaugino masses which is part of the minimal SUGRA framework, this is twice the chargino mass). This would correspond to parameter set 2 in our study. A study of a similar point has already been performed for the JLC detector [4].

In the case that we are studying, the neutralinos and charginos are light, so we choose to go down to 250 GeV in order to measure the masses of the neutralinos $\widetilde{\chi}_{1,2}^0$ and the chargino $\widetilde{\chi}_1^{\pm}$. These measurements are better at the lower energy, since it eliminates potentially confusing cascade decays and it improves the resolution of the mass measurement technique.

B. 250 GeV

At a center of mass energy of 250 GeV, the only sparticles that can be produced are the $\widetilde{\chi}_1^0$, $\widetilde{\chi}_2^0$ and $\widetilde{\chi}_1^{\pm}$. Table III lists the production cross sections at this energy.

Table III: Production cross sections (in fb) for point 3 at $\sqrt{s}$ = 250 GeV with right- and left-handed polarized electrons.

Production mode	80% right		80% left	
$\widetilde{\chi}_1^+\widetilde{\chi}_1^-$	503	(35.0%)	1991	(68.7%)
$\widetilde{\chi}_1^0\widetilde{\chi}_1^0$	452	(31.5)	180	(6.2)
h^0Z^0	404	(28.1)	484	(16.7)
$\widetilde{\chi}_1^0\widetilde{\chi}_2^0$	63	(4.4)	183	(6.3)
$\widetilde{\chi}_2^0\widetilde{\chi}_2^0$	14	(1.0)	62	(2.1)
total	1436		2899	

1. *Properties of the chargino*

One study to be performed is the measurement of the cross sections for chargino production as a function of electron polarization. As Figure 12 indicates, for $\sqrt{s} \gg m_Z$, left-handed electrons can produce charginos whether or not the chargino is gaugino-like or Higgsino-like, while right-handed electrons can only produce charginos if the chargino is Higgsino-like. Thus, if $\sigma_L \gg \sigma_R$, then the chargino is gaugino-like; Table III indicates that this is the case in the SUGRA model we are using in our simulation.

By a Monte Carlo study we have determined that with 20 fb^{-1} of data, and 80% electron polarization, we can determine the left- and right-handed cross sections to

$$\frac{\delta\sigma}{\sigma}(P_L = +0.6) = 1.5\%$$
$$\frac{\delta\sigma}{\sigma}(P_L = -0.6) = 2.0\%$$

2. *Chargino and neutralino masses*

To measure the masses of the $\widetilde{\chi}_1^{\pm}$ and $\widetilde{\chi}_1^0$ we look at the chargino decays $\widetilde{\chi}_1^{\pm} \to \widetilde{\chi}_1^0 q\overline{q}$ and $\widetilde{\chi}_1^{\pm} \to \widetilde{\chi}_1^0 \ell^{\pm}\nu_{\ell}$ and the neu-

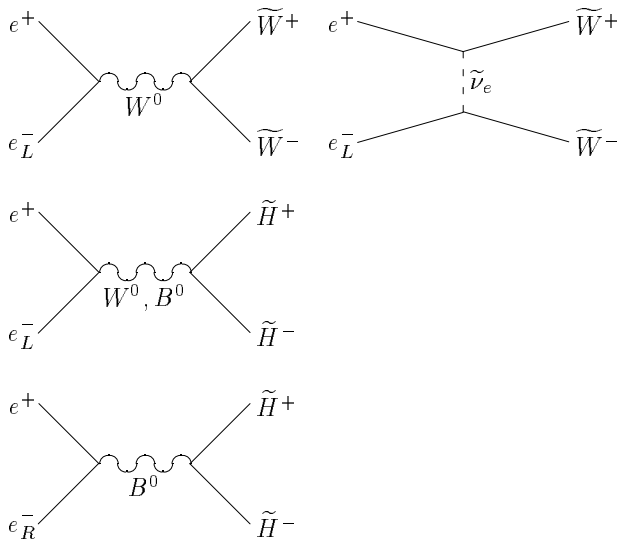

Figure 12: First order Feynman diagrams for $e^+e^- \to \widetilde{\chi}_1^+\widetilde{\chi}_1^-$, where $\widetilde{W}$ and $\widetilde{H}$ are the gaugino and Higgsino components of the chargino. The left-handed electron can couple to both the B^0 (the *U*(1) component of the Z-γ) and the W^0 (the *SU*(2) component); the right-handed electron can only couple to the B^0.

tralino decays $\widetilde{\chi}_2^0 \to \widetilde{\chi}_1^0 q\overline{q}$ and $\widetilde{\chi}_2^0 \to \widetilde{\chi}_1^0 \ell^+\ell^-$ using the procedure outlined in section III.B. Table IV shows that this exhausts the measurable possibilities for these sparticle decays.

Figure 13 shows the reconstructed jet-jet mass from $e^+e^- \to \widetilde{\chi}_1^+\widetilde{\chi}_1^- \to \widetilde{\chi}_1^0\ell^\pm\nu_\ell\widetilde{\chi}_1^0 q\overline{q}$ events, with cuts to select an isolated lepton in one hemisphere and jet pairs in the other. Figure 14 shows the results of the fit to the endpoint of the jet energy spectrum. With 20 fb^{-1} of data at 250 GeV the errors on the masses should be

$$\frac{\delta m_{\widetilde{\chi}_1^0}}{m_{\widetilde{\chi}_1^0}} = 1\%,$$

Table IV: Branching ratios of neutralinos and charginos at point 3.

Decay mode	Fraction
$\widetilde{\chi}_2^0 \to \widetilde{\chi}_1^0\ell^+\ell^-$	49.7%
$\to \widetilde{\chi}_1^0 q\overline{q}$	42.4
$\to \widetilde{\chi}_1^0\nu_\ell\overline{\nu}_\ell$	7.8
$\widetilde{\chi}_3^0 \to \widetilde{\chi}_1^\pm W^\mp$	58.6
$\to \widetilde{\chi}_1^0 Z^0$	22.2
$\to \widetilde{\chi}_1^0 h^0$	10.1
$\widetilde{\chi}_1^+ \to \widetilde{\chi}_1^0 q\overline{q}$	66.3
$\to \widetilde{\chi}_1^0\ell^+\nu_\ell$	33.7

Table V: Branching ratios of sleptons and squarks at point 3.

Decay mode	Fraction
$\widetilde{\nu}_e \to \widetilde{\chi}_1^+ e^-$	61.5
$\to \widetilde{\chi}_2^0\nu_e$	31.9
$\to \widetilde{\chi}_1^0\nu_e$	6.6
$\widetilde{e}_R^+ \to \widetilde{\chi}_1^0 e^+$	99.0
$\widetilde{e}_L^+ \to \widetilde{\chi}_1^+\overline{\nu}_e$	54.4
$\to \widetilde{\chi}_2^0 e^+$	24.2
$\to \widetilde{\chi}_1^0 e^+$	21.4
$\widetilde{t}_1 \to \widetilde{\chi}_1^+ b$	64.6
$\to \widetilde{\chi}_1^0 t$	35.4
$\widetilde{b}_L \to \widetilde{\chi}_2^0 b$	86.2
$\to \widetilde{\chi}_1^- t$	13.7

$$\frac{\delta m_{\widetilde{\chi}_1^\pm}}{m_{\widetilde{\chi}_1^\pm}} = 1\%.$$

Because the chargino cross-section depends on the sneutrino mass, this measurement allows us to predict that the mass of the sneutrino will be less than 250 GeV. This prediction is model independent; it holds for any choice of soft-supersymmetry breaking terms. Given these results the next step is to run the NLC at 500 GeV to study the masses of sneutrinos and the sleptons.

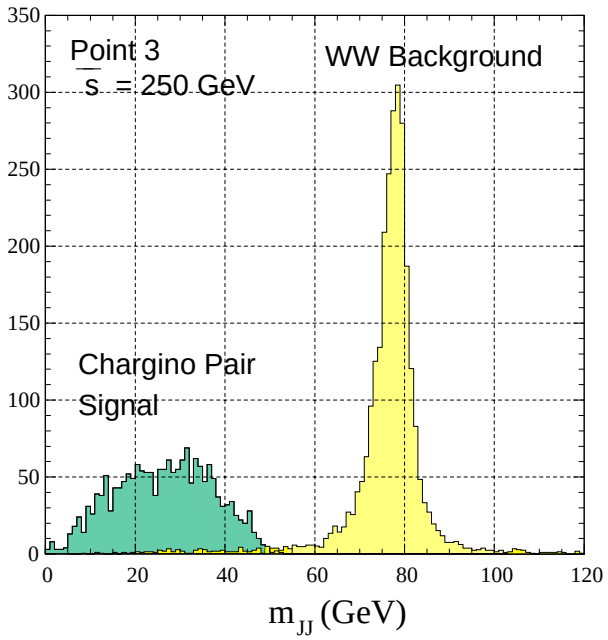

Figure 13: The jet-jet invariant mass from $\widetilde{\chi}_1^\pm \to \widetilde{\chi}_1^0 q\overline{q}$ events and from SM W^+W^- events.

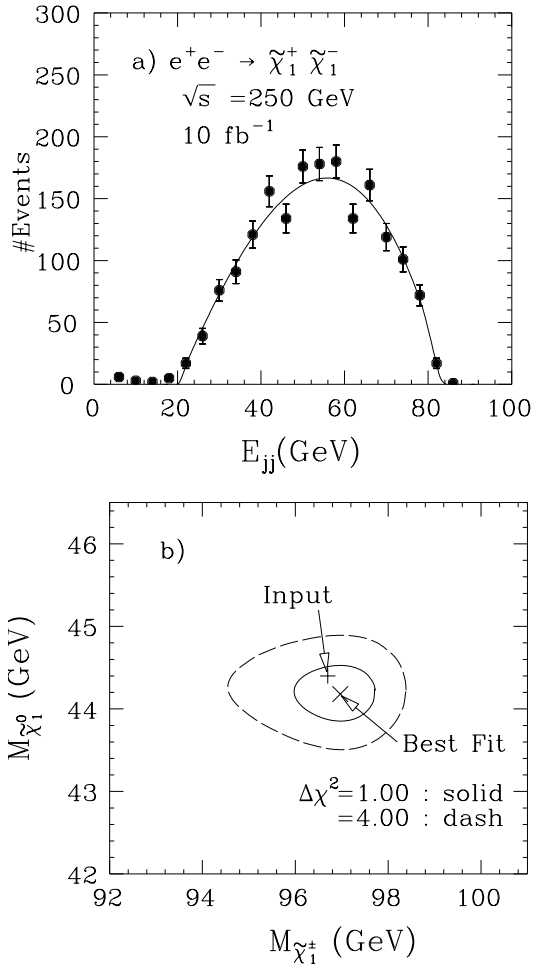

Figure 14: The jet energy spectrum, and the mass obtained from the fit to the spectrum.

Table VI: Production cross sections (in fb) for point 3 at $\sqrt{s}$ = 500 GeV.

Production mode	80% right		80% left	
$\tilde{\chi}_1^0\tilde{\chi}_1^0$	365	(26.4%)	151	(5.9%)
$\tilde{\nu}_e\tilde{\nu}_e$	252	(18.3)	978	(38.3)
$\tilde{e}_R^+\tilde{e}_R^-$	243	(17.6)	65	(2.5)
$\tilde{\chi}_1^+\tilde{\chi}_1^-$	159	(11.5)	640	(28.2)
h^0Z^0	59	(4.3)	72	(2.8)
$\tilde{\chi}_1^0\tilde{\chi}_2^0$	57	(4.1)	187	(7.3)
$\tilde{e}_L^+\tilde{e}_L^-$	44	(3.2)	158	(6.2)
total	1379		2551	

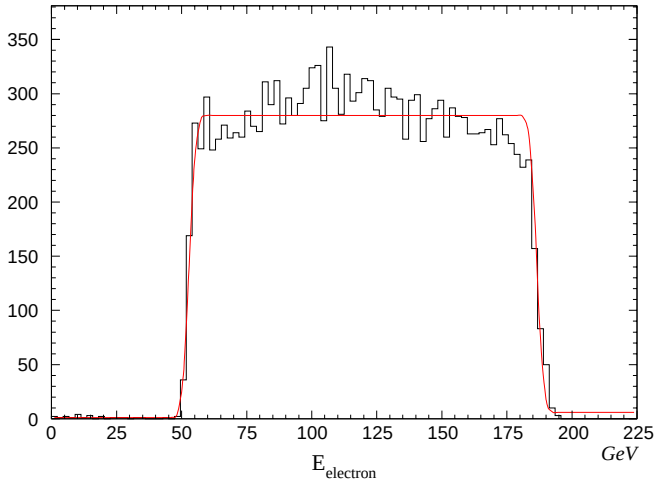

Figure 15: Distribution of electron energies from the decays of $\tilde{e}_R^\pm$. The fit is to a convolution of a box with a Gaussian. The endpoints of the distribution determine the selectron and neutralino masses.

C. 500 GeV

At 500 GeV, the energy is sufficient to produce sleptons and sneutrinos. According to Table VI, large numbers of $\tilde{e}_R^+\tilde{e}_R^-$ events will be produced; from Table V, we see that the decay $\tilde{e}_R^\pm \to \tilde{\chi}_1^0 e^\pm$ dominates. Thus the signal will be two isolated electrons and large missing energy.

Figure 15 shows the distribution of electron energies from the decay $\tilde{e}_R^\pm \to \tilde{\chi}_1^0 e^\pm$. The endpoints of the distribution determine the masses the $\tilde{e}_R^\pm$ and the $\tilde{\chi}_1^0$, as shown in Figure 16. In this example, the fit values of the parameters do not coincide exactly with the input values; this is partly due to background from other decays which distort the endpoints of the energy spectrum. Since this effect is correctable, the most important feature to notice is the size of the uncertainties in the masses. (To be conservative, however, we have taken the errors on the masses to be $\delta m_{\tilde{e}_R}$= 2 GeV and $\delta m_{\tilde{\chi}_1^0}$= 1.5 GeV. Note that the $\tilde{\chi}_1^0$ mass measurements from section IV.B could have been used to provide an additional constraint on the $\tilde{e}_R^\pm$ mass.)

With 20 fb^{-1} of data at 500 GeV for 80% right-handed electrons the errors on the masses should be

$$\frac{\delta m_{\tilde{\nu}_e}}{m_{\tilde{\nu}_e}} = 2\%,$$
$$\frac{\delta m_{\tilde{e}_R}}{m_{\tilde{e}_R}} = 1\%,$$
$$\frac{\delta m_{\tilde{\mu}_R}}{m_{\tilde{\mu}_R}} = 1.5\% \text{ and}$$
$$\frac{\delta m_{\tilde{e}_L}}{m_{\tilde{e}_L}} = 7\%.$$

The measurement of $m_{\tilde{e}_L}$ is difficult since the 2-electron final state is dominated by standard model background from $e^+e^- \to W^+W^- \to e^+\nu_e e^-\overline{\nu}_e$. Thus, we must look at the 6-electron final state from $\tilde{e}_L^\pm \to \tilde{\chi}_2^0 e^+ \to \tilde{\chi}_1^0 e^+ e^- e^+$, which has no standard model background but suffers from low statistics [10].

Given these measurements we can fit for the underlying supersymmetry parameters which describe the neutralino and chargino masses and mixings, namely M_1, M_2, μ and $\tan\beta$. If

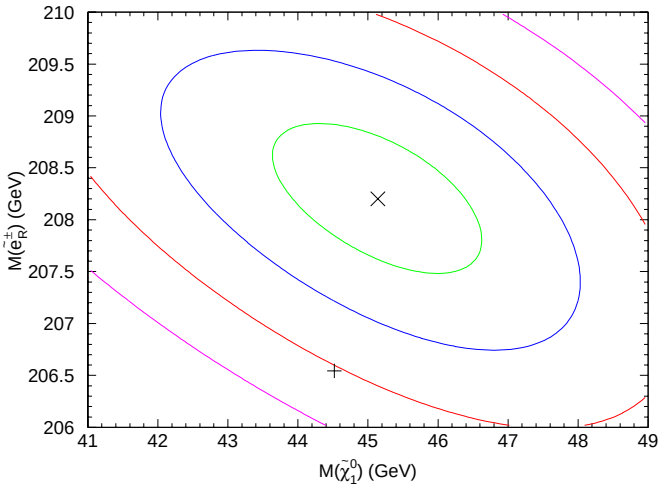

Figure 16: Reconstructed $\tilde{\chi}_1^0$ and $\tilde{e}_R^{\pm}$ masses, along with the input values. The contours are spaced at 1-σ intervals. The + represents the input values of the parameters (44.5 and 206.6 GeV) and the $\times$ represents the best fit values (45.1 and 208.2 GeV).

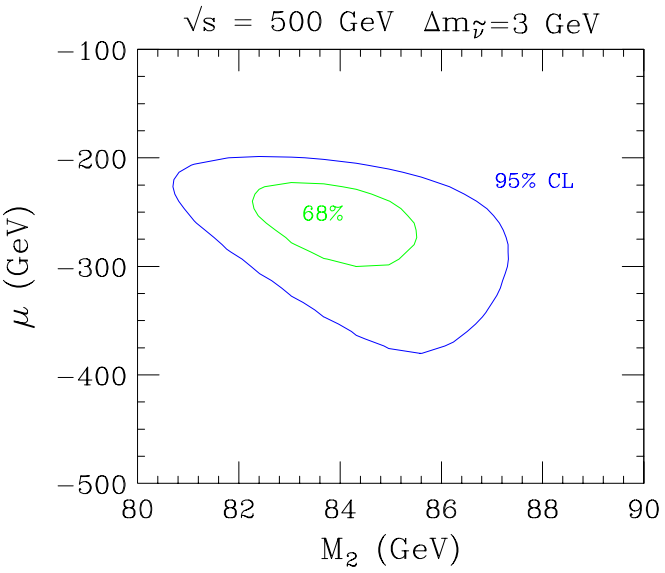

Figure 17: Errors on the measurement of μ and M_2 at $\sqrt{s} = 500$ GeV.

we assume the grand-unified assumption between M_1 and M_2, we determine (at 68% CL)

$$\begin{aligned} \frac{\delta M_2}{M_2} &= 1.5\% \\ \frac{\delta \mu}{\mu} &= 15\% \\ \tan\beta &= 2 \pm 0.35 \end{aligned}$$

We illustrate the χ^2 contours in Figures 17 and 18.

If we combine the measurements of the slepton masses with the SUGRA assumption, then we can predict that the squark masses are $m_{\tilde{q}} = 322 \pm 7$ GeV. We can run the NLC at 800 GeV to verify this prediction. We can also measure the properties of the heavy neutralino and chargino masses at this energy.

D. 800 GeV

To obtain measurements of the heavier SUSY particles, we run the NLC at 800 GeV. Table VII lists the production cross sections for point 3 at 800 GeV.

At a center of mass energy of 800 GeV it is relatively easy to devise a set of cuts which isolate a sample of primarily squark events. One of the cuts we applied requires the observation of two b-jets. Hence our sample is dominated by $\tilde{t}$ and $\tilde{b}$ production. Figure 19 shows the reconstructed jet energy for selected events in 50 fb^{-1} of data with 80% right polarization. Because a large fraction of the decays are two-body decays ($\tilde{b} \to b\tilde{\chi}^0$ and $\tilde{t} \to b\tilde{\chi}^+$) the jet energy distribution can be used to derive a generic squark mass of 307 GeV, using the standard endpoint technique. This value lies in the middle of the range of squark masses for the comparison point and amounts to a 10% measurement of the squark mass.

The final step in this analysis, which we will not detail in this report, would entail running the NLC at $\sqrt{s} = 1000$ GeV to measure the properties of the heavy Higgs boson and heavy top-squark.

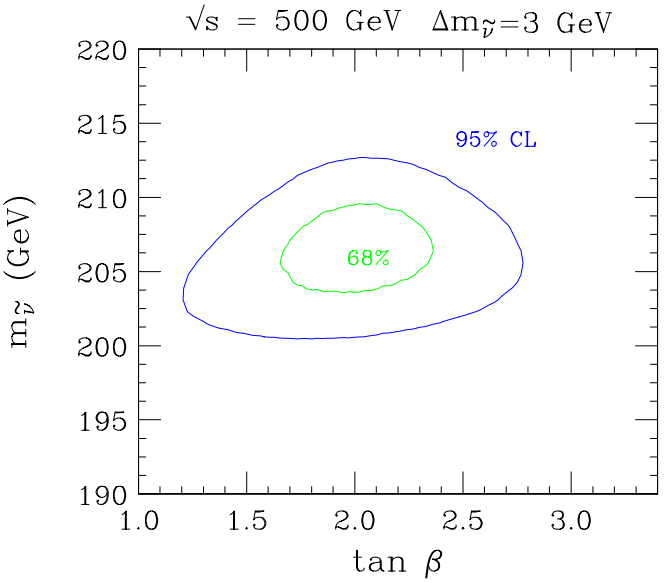

Figure 18: Errors on the measurement of $M_{\tilde{\nu}}$ and tan(β) at $\sqrt{s}$ = 500 GeV.

V. TESTS OF SUPERSYMMETRY

In the previous section techniques were described to measure supersymmetric masses and mixing angles such as $m_{\tilde{\nu}}$, $\tan\beta$, etc. In the process of this extraction we have made very few model assumptions. Implicit in the analysis, however, was the assumption that the new phenomena measured is indeed origi-

Table VII: Selected production cross sections (in fb) for point 3 at $\sqrt{s} = 800$ GeV. The symbol $\tilde{q}$ represents all first- and second-generation squarks.

Production mode	80% right		80% left	
$\tilde{e}_R^+\tilde{e}_R^-$	538	(27.6%)	142	(3.8%)
$\tilde{\nu}_e\tilde{\nu}_e$	434	(22.3)	1687	(45.7)
$\tilde{\chi}_1^0\tilde{\chi}_1^0$	210	(10.8)	83	(2.2)
$\tilde{e}_L^+\tilde{e}_L^-$	123	(6.3)	467	(12.6)
$\tilde{\chi}_2^+\tilde{\chi}_2^-$	98	(5.0)	245	(6.6)
$\tilde{\chi}_1^+\tilde{\chi}_1^-$	89	(4.6)	356	(9.6)
$\tilde{q}\tilde{q}$	71	(3.7)	128	(3.5)
$\tilde{\chi}_3^0\tilde{\chi}_4^0$	58	(3.0)	70	(1.9)
$\tilde{t}_1\tilde{t}_1$	28	(1.4)	17	(0.5)
$\tilde{b}_L\tilde{b}_L$	11	(0.6)	36	(1.0)
total	1945		3693	

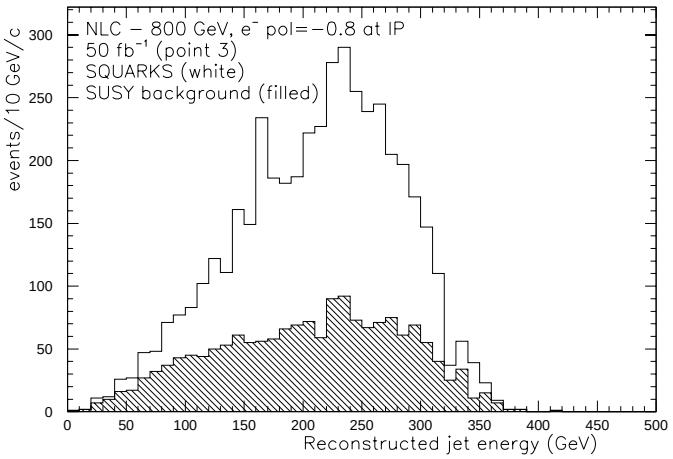

Figure 19: The energy distribution of squarks and background from other SUSY processes at $\sqrt{s} = 800$ GeV.

nating from supersymmetry with minimal particle content. In this section, we describe some experiments at the NLC which allow us to test this assumption.

A powerful hint for supersymmetry would be discovery of new particles which have the correct quantum numbers to be supersymmetric partners of the standard model particles. Nevertheless, it would only be a strong hint and not "proof" that nature is supersymmetric. More compelling evidence can be provided by looking at the couplings of different operators which are related by supersymmetry invariance. Just as gauge invariance forces relations among interactions, so does supersymmetry invariance. One example of these relations is

$$g_2 W_\mu^+ \bar{\nu}_L \gamma_\mu e_L \leftrightarrow g_2 \tilde{W}^+ e_L \tilde{\nu}^* \qquad (1)$$

If supersymmetry were not realized then there would be no symmetry principle requiring that the g_2 coupling on the left side be equal to the g_2 coupling on the right side.

It is useful to call the g_2 on the RHS of Eq. 1 g_2^χ and then experimentally test whether $g_2^\chi = g_2$. One of the most effective ways to make this test is in the production of $e_L^- e^+ \to \chi_1^+\chi_1^-$ [13]. The Feynman diagrams for this production process are contained in Figure 12. Here, a t channel diagram exchanging a $\tilde{\nu}_e$ contains the coupling g_2^χ at the electron-sneutrino-chargino vertex. The amplitude for this diagram is

$$A_{\tilde{\nu}} \sim \frac{|g_2^\chi V_{11}|^2}{t - m_{\tilde{\nu}}^2}.$$

(The V_{11} factor is simply how much $\tilde{W}^-$ is contained in the lightest chargino eigenstate.) Since this amplitude depends on three quantities, g_2^χ, V_{11} and $m_{\tilde{\nu}}$, it is necessary to use three observables to pin down g_2^χ. In Ref. [13] the three observables were taken to be the total cross-sections $\sigma_{L,R}(\chi^+\chi^-)$ and the asymmetry,

$$A_L^\chi \equiv \frac{\sigma_L(0 < \cos\theta < 1/\sqrt{2}) - \sigma_L(-1 < \cos\theta < 0)}{\sigma_L(-1 < \cos\theta < 1/\sqrt{2})}.$$

The example model studied in [13] sets

$$(\mu, M_2, \tan\beta, m_{\tilde{l}}, m_{\tilde{q}}) = (-500, 170, 4, 400, 700)$$

which produces gaugino mass eigenstates of $m_{\chi_1^\pm} = 172$ GeV, $m_{\chi_2^\pm} = 512$ GeV, and $m_{\chi_1^0} = 86$ GeV. $V_{11} \simeq 1$ is determined by measuring $\sigma_R \simeq 0$, and the other two parameters are determined by σ_L and A_L^χ. Figure 20 plots the allowed bands in the g_2^χ/g_2 vs. $m_{\tilde{\nu}}$ plane which are consistent with σ_L (solid curves) and A_L^χ (dashed curves) at 100 fb^{-1} of integrated luminosity. The shaded regions are consistent with both observables and constitute the allowed regions. The authors conclude that g_2^χ could be measured to

$$0.85 \leq g_2^\chi/g_2 \leq 1.3.$$

A determination of g_2^χ this close to g_2 is a good quantitative test that supersymmetry is realized in nature. The analysis also predicts $m_{\tilde{\nu}} \simeq 400$ GeV. Tuning the center of mass energy sufficient to directly detect this particle and measuring its mass near 400 GeV would greatly strengthen the claim for supersymmetry. The direct measurement of $m_{\tilde{\nu}}$ could then be used in the analysis to test $g_2 = g_2^\chi$ to better than 5%.

Other tests similar to the one described above can be performed to verify supersymmetry. For example, supersymmetry invariance relates

$$g_2 W_\mu^- H^+ \bar{\partial}^\mu H_u^0 \quad \leftrightarrow \quad g_2 \langle H_u^0 \rangle \tilde{W}^- \tilde{H}^+ .$$

The RHS is a term in the chargino mass matrix mixing the wino and Higgsino fermions. This mixing term is proportional to

$$g_2 \langle H_u^0 \rangle \propto m_W \sin\beta,$$

and affects both the mixing angles and mass eigenvalues of the physical chargino states. One can replace m_W with m_W^χ, and $\tan\beta$ with $\tan\beta^\chi$ and measure them independently using the full complement of chargino observables. If $m_W^\chi = m_W$, which can be tested [13], then supersymmetry has passed another test.

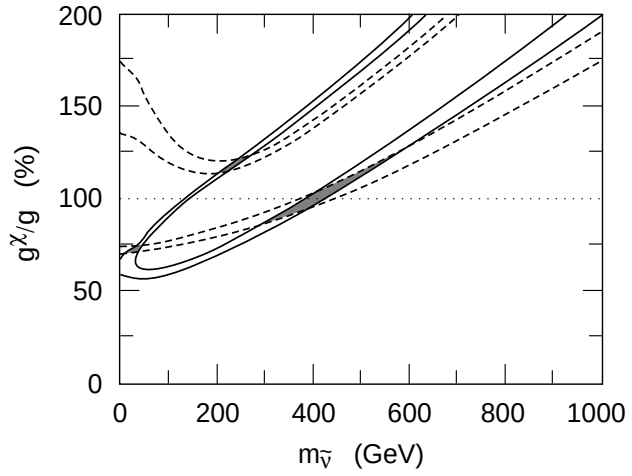

Figure 20: The allowed bands in the g_2^{χ}/g_2 vs. $m_{\tilde{\nu}}$ plane.

More precise tests of supersymmetry have been suggested by [14] using slepton pair production. The production cross-section for $\tilde{e}_R^+\tilde{e}_R^-$ is sensitive to t-channel $\widetilde{B}$ exchange. The coupling of the $\widetilde{B}$ to the electron and right-handed selectron is related by supersymmetry to the coupling between the B_μ gauge field and two electrons: $g_{\tilde{B}\tilde{e}_R e_R} = \sqrt{2}g'$. Precise measurement of the $\tilde{e}_R\tilde{e}_R$ cross sections then enables a precise test of this relation, and an extraction of M_1 (see Figure 21). In [14] this test was illustrated with the following underlying parameter choices: $m_{\tilde{e}_R} = 200$ GeV, $\mu = 300$ GeV, $M_1 = 99.57$ GeV, and $\tan\beta = 2$. With $\sqrt{s} = 500$ GeV and 100 fb^{-1} of data the equality of these couplings can be tested to better than 2% accuracy.

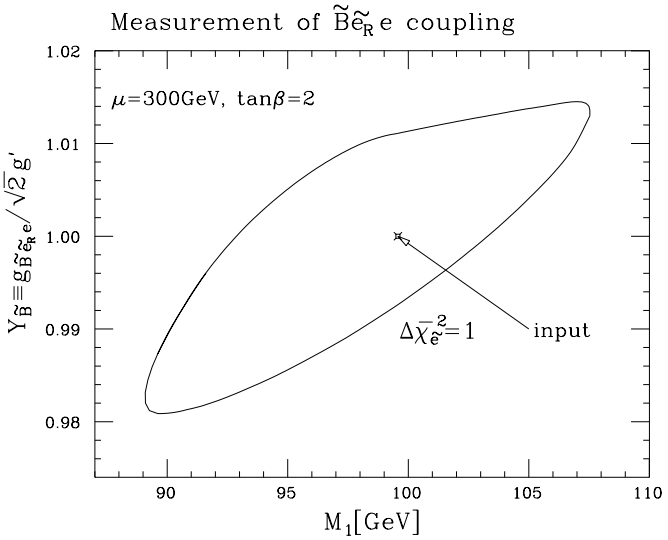

Figure 21: Test of SUSY from the selectron distribution [14].

Since supersymmetry cannot be an exact symmetry of nature, one does not expect these equalities among the couplings discussed above to hold at arbitrary precision. Indeed, small deviations of $\mathcal{O}(1\%)$ in these relations are expected to manifest themselves due to logarithmic sensitivity to the decoupling of higher mass supersymmetric states. The test described above is so precise that it begins to be sensitive to these tiny deviations in the relation between $g_{\tilde{B}\tilde{e}_R e_R}$ and g' due to supersymmetry breaking. With more luminosity it is even perhaps possible to extract a rough estimate of the squark mass scale from this measurement [14].

Once supersymmetry has been established the next most important question to answer is *what is the mechanism underlying supersymmetry breaking?* There is no compelling model for a pattern to the soft supersymmetry breaking masses which make all the scalars and gauginos heavy, except that they must satisfy gauge invariance in the full Lagrangian. Since the NLC can directly measure the gaugino and scalar masses with high precision, experiments at the NLC will provide invaluable guidance that may help uncover the physics of SUSY breaking, and thus distinguish between various theoretical approaches [2].

We discuss briefly two examples of mass relations that would be extremely valuable to know to make sense of the theory. The first relation is between the gaugino masses. Grand unified theories (GUT), which typically have a unified gaugino mass at the GUT scale, make definite predictions for the mass ratios of the different gauginos. Renormalization group equations to one loop predict that

$$\frac{M_i(Q)}{\alpha_i(Q)} = \text{scale independent.}$$

Since all the M_i unify to $m_{1/2}$ at the GUT scale and all the α_i unify to α_G at the GUT scale, one can make the prediction that

$$M_2 \equiv \frac{\alpha_2(m_Z)}{\alpha_1(m_Z)} M_1 \simeq 2M_1 .$$

This is commonly referred to as the "GUT relation between M_1 and M_2." Other models of supersymmetry which do not incorporate grand unification also may predict this "GUT relation" [2]. The principle of supersymmetry does not dictate any relation between M_1 and M_2 and so it is an experimental question to find out if $M_2/M_1 \simeq 2$.

An example of this kind of test was given in [4]. The set of parameters they studied was

$$(\mu, M_2, \tan\beta, m_{\tilde{l}_R}, m_{\tilde{l}_L}) = (400, 250, 2, 142, 236). \qquad (2)$$

With 20 fb^{-1} of data at $\sqrt{s} = 350$ GeV and 50 fb^{-1} of data at $\sqrt{s}$ = 500 GeV, the *independent* values of M_1 and M_2 can be disentangled. Figure 22 illustrates this test with contours of $\Delta\chi^2 =$ 1 (dash), 2.28 (dot-dash) and 4.61 (solid).

Studying the scalar mass spectroscopy can also provide useful information about the underlying theory of supersymmetry. As an example, we can write down the difference between the low energy physical masses $\tilde{e}_L$ and $\tilde{e}_R$ as

$$m^2_{\tilde{e}_L} - m^2_{\tilde{e}_R} = m^2_L - m^2_E + C_2 - \frac{3}{4}C_1 + (-\frac{1}{2} + 2\sin^2\theta_W) m_Z^2 \cos 2\beta \quad (3)$$

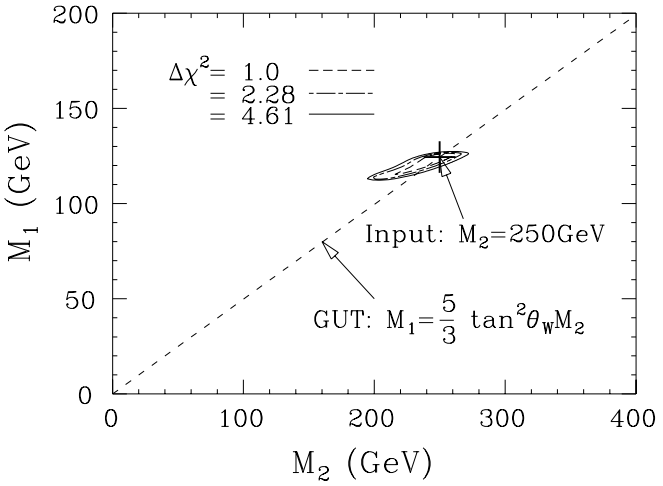

Figure 22: M_1 and M_2 measurement based on a global fit to M_1, M_2, μ, and $\tan\beta$ [4]. The dashed line indicates the GUT prediction.

where m_L^2 and m_E^2 represent the soft mass term at the "boundary condition scale" and the C_i's are contributions induced by gaugino-mass loops in the renormalization group equations. The precise definitions of C_i's at one loop are given, for example, in Ref. [15]. The last term proportional to m_Z^2 are D-term contributions to the slepton physical masses and are numerically insignificant here.

To illustrate the distinguishing power of the above relation between $\tilde{e}_L$ and $\tilde{e}_R$ we detail the values of each of the terms on the RHS of Eq. 3 for three different models: (a) mSUGRA with universal scalar masses at the GUT scale, (b) *SU*(5) GUT with the $\tilde{e}_L$ in a $\overline{5}$ representation of *SU*(5) with its own soft mass term and the $\tilde{e}_R$ in a 10 representation of *SU*(5) with its own soft mass term at the GUT scale, and (c) minimal gauge mediated (MGM) model of supersymmetry breaking which has a "boundary condition scale" for the soft masses much lower in scale than the supergravity theories of (a) and (b). This "boundary condition scale" in the MGM is usually called the messenger scale, M, and is typically $\mathcal{O}(10^5$ GeV$)$.

In these three theories,

$$m_{\tilde{L}}^2 - m_{\tilde{E}}^2 = \begin{cases} 0, & \text{mSUGRA} \\ m_5^2 - m_{10}^2, & \textit{SU}(5)\text{ GUT} \\ \left\{ \frac{3}{2}\left(\frac{\alpha_2(M)}{\alpha_2(m_Z)}\right)^2 M_2^2 \right. & \\ \qquad \left. - \frac{9}{10}\left(\frac{\alpha_1(M)}{\alpha_1(m_Z)}\right)^2 M_1^2 \right\}, & \text{MGM} \end{cases}$$

and

$$C_2(m_Z) - \tfrac{3}{4}C_1(m_Z) = \begin{cases} \left\{ \frac{3}{2}M_2^2\left[\frac{\alpha_G^2}{\alpha_2^2(m_Z)} - 1\right] \right. & \\ \qquad \left. - \frac{3}{22}M_1^2\left[\frac{\alpha_G^2}{\alpha_1^2(m_Z)} - 1\right]\right\}, & \begin{matrix}\text{mSUGRA or} \\ \textit{SU}(5)\text{ GUT}\end{matrix} \\ \left\{ \frac{3}{2}M_2^2\left[\frac{\alpha_2^2(M)}{\alpha_2^2(m_Z)} - 1\right] \right. & \\ \qquad \left. - \frac{3}{22}M_1^2\left[\frac{\alpha_1^2(M)}{\alpha_1^2(m_Z)} - 1\right]\right\}, & \text{MGM} \end{cases}$$

where $\alpha_G \simeq 0.04$ is the value of the gauge couplings at the GUT scale. In each model the "GUT relation" $M_2 \simeq 2M_1$ holds. Therefore, we can get an approximate numerical relationship between the selectron masses and M_2:

$$m_{\tilde{e}_L}^2 - m_{\tilde{e}_R}^2 \simeq \begin{cases} 0.5M_2^2, & \text{mSUGRA} \\ m_5^2 - m_{10}^2 + 0.5M_2^2, & \textit{SU}(5)\text{ GUT} \\ 1.4M_2^2. & \text{MGM} \end{cases}$$

In Figure 23 the relation between M_2 and $m_{\tilde{e}_L}^2 - m_{\tilde{e}_R}^2$ is plotted. The line in the figure is the approximate relation expected in the mSUGRA model (solid) and the MGM model (dashed). Since m_5^2 and m_{10}^2 can be arbitrary masses, a single line cannot be drawn in the figure for the *SU*(5) GUT model. However, any line parallel to the solid line could in principle describe the *SU*(5) GUT mass pattern. Any point above the solid line would be consistent with $m_5 > m_{10}$, and everything below the solid line would be consistent with $m_{10} > m_5$. Using the same set of parameters as given by Eq. 2, it was found that using 20 fb^{-1} of data at $\sqrt{s} = 350$ and 400 GeV and 50 fb^{-1} of data at $\sqrt{s} = 500$ GeV, the $m_{\tilde{e}_L}$ and M_2 masses could be measured to better than 2% and 5% respectively. The cross-hairs in the figure are the equivalent 1σ errors in the measured values of M_2 and $\sqrt{m_{\tilde{e}_L}^2 - m_{\tilde{e}_R}^2}$. The cross hairs nicely fall on the mSUGRA line, providing further evidence that the model has unified slepton masses at the GUT scale.

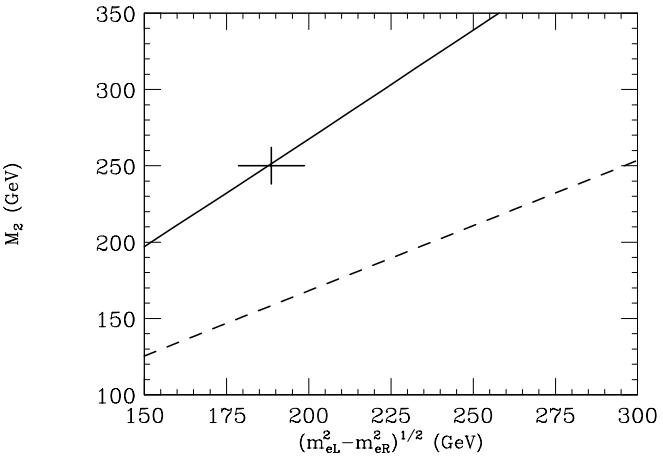

Figure 23: The relation between M_2 and $m_{\tilde{e}_L}^2 - m_{\tilde{e}_R}^2$.

The hypothesis of mSUGRA is an especially simplifying one. It reduces the over 120 independent parameters needed to describe the MSSM to five parameters: m_0, $m_{1/2}$, $\tan\beta$, sign(μ), and A_0. Neglecting the potentially difficult non-linearities, as few as five independent observables involving supersymmetric particles need be measured to pin down all of these input parameters. Using the results from the previous sections on the determinations of $m_{\tilde{\chi}^0_{1,3}}$, $m_{\tilde{\chi}^\pm_1}$, $\sigma_{L,R}(\tilde{\chi}^+_1\tilde{\chi}^-_1)$, $m_{\tilde{e}_{L,R}}$, we construct a total χ^2 for point 3 and vary over all the input parameters to find the best fit to the data. The best fit to the data of course corresponds to the input parameters of point 3 with errors,

$$\delta m_0 \quad = \quad {}^{+2.7}_{-2.7}\text{ GeV}$$

$$\begin{aligned} \delta m_{1/2} &= {}^{+2.5}_{-1.0}\ \text{GeV} \\ \delta \tan\beta &= {}^{+0.17}_{-0.31} \\ \text{sign}(\mu) &= \text{determined}. \end{aligned}$$

The precise determination of these parameters then can be used to cautiously predict other observables such as the squark masses, heavy gauginos, and heavy Higgses.

Finally, if one were to assume at the outset that nature is described by an mSUGRA model, then one can try to interpret all measurements in only this framework and simply wait for a large deviation to appear before discounting the model. That is, a χ^2 can be formulated, as is currently done in the standard model, which incorporates all the observables which are measurable at NLC, and as long as the χ^2 remains sufficiently small then we maintain confidence in the mSUGRA model. Planning an experimental program based on this notion is naive since mSUGRA is approximately a measure zero set of all the viable alternatives in supersymmetry. It is therefore vital that one can iterate through a model independent analysis to *determine experimentally* what the underlying weak-scale parameters of the theory are, rather than making numerous simple hypotheses hoping that the postulated theory can then be verified.

VI. CONCLUSIONS

In this paper, we have considered general methods for discovering supersymmetry and measuring the properties of supersymmetric particles at the NLC. In particular, we have explored one specific model of SUSY and shown how the NLC can be used to fully reconstruct the parameters of the model.

The NLC will be essential to fully explore supersymmetry if it should exist, and offers the unique potential to make precision measurements that would allow us to begin to explore physics at still higher energy scales, perhaps all the way to the scale at which the forces of nature are unified.

VII. REFERENCES

[1] H. P. Nilles, Phys. Repts. **110**, 1 (1984); J. L. Lopez, DOE/ER/40717-23 (hep-ph/9601208), to appear in Rept. Prog. Phys.

[2] J. Amundson *et al.*, "Report of the Supersymmetry Theory Subgroup," these proceedings.

[3] H. Baer, R. Dubois, S. Fahey, S. Manly, R. Munroe, U. Nauenberg, X. Tata, D. L. Wagner, Determination of Supersymmetric Particle Production Cross Sections and Angular Distributions at a High Energy Linear Collider, contributed paper to *Physics and Technology of the Next Linear Collider*, BNL 52-502, Fermilab-PUB-96/112, LBNL-PUB-5425, SLAC Report 485, UCRL-ID-124160, submitted to the Snowmass '96 conference.

[4] T. Tsukamoto, K. Fujii, H. Murayama, M. Yamaguchi, and Y. Okada, Phys. Rev. D **51**, 3153 (1995).

[5] F. Paige, S. Protopopescu, in *Supercollider Physics*, p. 41, edited by D. Soper (World Scientific, 1986); H. Baer, F. Paige, S. Protopopescu, and X. Tata in *Proceedings of the Workshop on Physics at Current Accelerators and Supercolliders*, edited by J. Hewett, A. White, and D. Zeppenfeld, (Argonne National Laboratory, 1993), hep-ph 9305342.

[6] T. Sjöstrand, *Comp. Phys. Comm.* **82**, 74 (1994).

[7] S. Mrenna, *Simulating Supersymmetry with PYTHIA*, ANL-HEP-PR-96-63.

[8] H. Baer, C. H. Chen, R. Munroe, F. Paige and X. Tata, Phys. Rev. D **51**, 1046 (1995).

[9] H. Baer, A. Bartl, D. Karatas, W. Majerotto and X. Tata, Int. J. Mod. Physics, A **4**, 4111 (1989).

[10] H. Baer, R. Munroe and X. Tata, *Supersymmetry Studies at Future Linear e^+e^- Colliders*, FSU-HEP-960601 (1996) (hep-ph/0906325).

[11] S. Kuhlman *et al.*, *Physics and Technology of the Next Linear Collider*, BNL 52-502, Fermilab-PUB-96-112, LBNL-PUB-5425, SLAC Report 485, UCRL-ID-124160, submitted to the Snowmass '96 conference.

[12] *Zeroth-Order Design Report for the Next Linear Collider*, LBNL-PUB-5424, SLAC Report 474, UCRL-ID-124161.

[13] J. L. Feng, M. E. Peskin, H. Murayama, X. Tata, Phys. Rev. D **52** (1995) 1418.

[14] M. Nojiri, K. Fujii, and T. Tsukamoto, KEK Preprint 96-41 (hep-ph/9606370), to appear in Phys. Rev. D.

[15] S. Martin, P. Ramond, Phys. Rev. D48 (1993) 5365.